Key Engineering Materials *Online: 2008-06-17*
ISSN: 1662-9795, Vol. 384, pp 283-309
doi:10.4028/www.scientific.net/KEM.384.283

Electroplated nickel composites with micron- to nano-sized particles

Bernhard Wielage [a], Thomas Lampke, Manuela Zacher, Dagmar Dietrich

Chemnitz University of Technology, Institute of Composite Materials and Surface Technology,

D-09107 Chemnitz, Germany

[a]bernhard.wielage@mb.tu-chemnitz.de

Keywords: electroplating, nanocomposite microstructure, electrochemical corrosion, Martens hardness, abrasion wear, fretting corrosion, cavitation wear, fatigue

Abstract. Electroplated nickel coatings provide ductility, excellent corrosion resistance and good wear resistance, which qualifies them to meet complex demands of engineering, microtechnology and microelectronics. The co-deposition of particles is a promising alternative to deposit layers with adequate microstructure and properties avoiding the rise of residual stress. The incorporation of the sufficient quantity of particles, monodisperse distribution and downsizing to nanometre scale affect the amount of strengthening by dispersion hardening. To avoid agglomeration in the electroplating bath as well as in the layer is a challenge which has been met by simple Watts nickel electrolyte with a minimum of organic additives and adequate bath agitation comprising sonication, i.e. the exposure of the bath to high-frequency sound waves.

Well-dispersed hard particles (titanium oxide and silicon carbide) were incorporated in nickel films. The focus was set on the correlation between the gained microstructure of the composites with particles from micron to nanometre scale and the electrochemical and mechanical properties. Corrosion was quantified from polarisation curves and volumetric erosion measurements. Wear resistance was evaluated by scratch energy density studies, oscillating sliding wear testing and cavitation wear testing and compared to indentation hardness results.

Sonication and particle downsizing result in matrix grain refinement and dispersion hardening. Incorporation of different particles with respect to different material and size proved to meet different demands. Submicron TiO_2 is best for high corrosion resistance, sonicated nickel without particle incorporation is best for high abrasion resistance, nano TiO_2 is best for oscillating sliding wear resistance and submicron SiC is best for cavitation wear resistance.

Introduction

Construction units are caught in the crossfire of complex loads (mechanical, thermal, tribological and corrosive) which arise in particular at the surface. The base materials are often not able to stand these loads, so that the construction units or components have to be coated. Nickel coatings, for example, are used for a variety of engineering purposes. Thus, nickel is used on moulds to provide durability, on coins, jewellery and circuit boards as a barrier layer, on strip steel, in piping systems and in aerospace applications for low stress or for re-sizing, and nevertheless in composites where a dispersed inorganic phase is co-deposited. Due to the ductility of the metal matrix, electroplated nickel dispersion films can combine good anti-corrosive behaviour with enhanced wear resistance because of the hardness and strengthening of incorporated non-metallic, mostly ceramic particles like alumina, titania or silicon carbide [1]. The composite material remains ductile and retains the deformability of the nickel matrix. Moreover, embedded particles can be selected to fulfil specific mechanical, electrical, piezoelectric, magnetic and even fluorescent or photocatalytic [2] properties in the coating.

Dispersion coatings have been known since the nineteenth century. For example, copper graphite layers for car engine components were tested in 1928 and the commercial production of nickel dispersion layers has been practised since the late 1950s [3]. In the following years, a lot of attention was paid to the more scientific aspects of composite plating related to the understanding and the modelling of the deposition process. So in 1972, Guglielmi developed the first model to

explain the co-deposition of ceramic particles from a sulphamate bath [4]. In that two-step model the particles were loosely adsorbed at the electrode in the first step. In the second step the particles were irreversibly adsorbed under the influence of an electric field. That hypothesis was the starting point for numerous scientists to develop further models [5]. The co-deposition of micron-sized particles of up to 15 % by volume has been state of the art for some years [6]. Currently, composite coatings with nanometre-sized particles are attaining the centre of interest particularly with regard to microelectronics, micro-electromechanical systems and precision engineering [7-9], where applications in contacts, interconnections of integrated circuits, motion elements or bearings are considered.

Unfortunately, especially co-deposited nanometre-sized particles in nickel films tend to agglomerate, which is undesirable with respect to the materials property. Hence, a sufficient dispersion of the particles in the electrolyte during electroplating must be reached, which is possible by application of ultrasonic energy to the galvanic bath in addition to the usual stirring against sedimentation of the particles. In any case, electrodeposition of pure metals under the influence of ultrasound has received significant attention for some years, as sonication can confer various benefits over conventional silent plating such as increased hardness, improved deposition rate, and greater adhesion of the substrate. These effects are attributed to increased transport of active species to the electrode surface by acoustic streaming, to continuous activation of the electrode and to ultrasonic degassing of the electrolyte. Application of low ultrasound frequencies in the range from 20 to 400 kHz decrease the thickness of the electrolyte double layer which forms at the metal-solution interface. The increase in mass transport changes the diffusion-controlled process to a charge-controlled process [10, 11]. In water, the main component of a Watts electrolyte, cavitation by means of an acoustic pressure field is the main effect for these frequencies. The occurring cavitation events release mechanical energy during the collapse of the resonance bubbles, producing microstreaming and shock waves [12]. The resulting shear stress is utilized for diverse procedures like cleaning, emulsifying or milling, i.e. to disperse sludge [13] and desagglomerate particles in solutions [14, 15].

Besides the identification of plating parameters, attention was paid to the understanding of how the corrosion and wear properties correlate with the microstructure of the particle-strengthened nickel composite. As referred to above, the mass transfer of reactants and products in the solution is enhanced through ultrasonic vibration and should affect the crystalline growth [16]. Since ultrasonic application is a key to incorporate nanoparticles in a fine-dispersed manner, the additional influence on matrix crystallisation (crystal morphology, mean grain size, formation of textures) was studied first by means of EBSD to differentiate between the influence of ultrasound and particle incorporation.

Most research on electrodeposited nickel dispersion coatings was focused on wear properties rather than on corrosion. Pure nickel coatings show an excellent resistance to corrosion in many environments (atmosphere, alkalis, melted hydroxides, diluted non-oxidising mineral acids) as well as at high temperatures up to 875 °C, which results from the ability to develop an oxide layer on the surface [17]. However, exposed to a chloride-containing medium, local corrosion cells arise on the nickel surface since chlorine ions hinder the formation of the protecting oxide layer. The latest research results have revealed that SiC and Al_2O_3 nickel composite coatings show a better corrosion resistance in 0.3 mol respectively 0.6 mol NaCl solutions than nickel coatings deposited under the same conditions [18]. The surface of dispersion coatings partially consists of incorporated ceramic particles; the exposed metallic area is diminished. Dielectric Al_2O_3 particles facilitate the formation of a passive layer on the nickel surface and the corrosion resistance improves the smaller the particles are and the more even their distribution is. [17]. The corrosion process proceeds in nickel along the grain boundaries and in composites particularly along the matrix/particle interfaces. The incorporated particles also change the microstructure of the matrix and thus the corrosion paths. Embedded micron-scaled SiC particles (5 μm diameter) cause minor disorder of the columnar nickel grain growth, whereas smaller SiC particles (0.3 μm diameter) produce a fine-grained equiaxed nickel matrix without crystallographic texture [19]. The residual tensile stresses decrease

the smaller the embedded particles are. In contrast, other papers report that disordering of the grain growth due to particle embedding leads to defects and higher internal stresses in the coatings [20-22]. If conducting particles are incorporated, the corrosion behaviour depends on their electrochemical potential [19, 23, 24]. Less work was done on corrosion studies of nickel reinforced with highly isolating TiO_2 particles. For a correlation between size and conductivity of incorporated particles and the corrosion behaviour of nickel dispersion coatings, semi-conducting SiC and isolating TiO_2 from micron to nanometre size are studied in this work.

Improved wear resistance of nickel composites by particle strengthening has been studied for decades. For automotive aluminium engines, nickel composite layers with silicon carbide particles respectively lubricating particles are state-of-the-art [25] and, for example, the long-life performance of Formula 1 race engines are enabled by such composite layers [26]. SiC-, Al_2O_3- and diamond-strengthened coatings are characterised by a high hardness and wear resistance [27-31]. Ni-TiO_2 layers increase the economic life-time of twist drills [32]. With the increasing availability of nanoparticles in the last years, the interest in nanoparticle-strengthened dispersion layers has been growing. The nano-scaled solids enable the application in construction units of micromechanics, e.g. as movement elements and bearings. Moreover, since nanoparticles can prevent dislocation movements at grain boundaries and thus recrystallisation procedures at elevated temperatures, microhardness and thermal stability are increased markedly. Recently, the idea has been developed to partially replace electrodeposited chromium coatings by nano-structured nickel dispersion coatings [30]. Regarding the practice, different wear types such as abrasion, impact and fretting as well as cavitation and jet wear occur according to the actual stress which consequently requires adapted wear tests for investigation. For this paper, the scratch test, the oscillating sliding wear test and the cavitation test were applied to study different wear behaviours.

The scratch test was primary developed for testing the adhesion of thin films. A good criterion for wear evaluation is the scratch energy density, i.e. the ratio of the tangential force and the scratch cross-sectional area [33]. The observation of other failure events such as cracks, chip formation and cohesive damage within the coating is important to determine the behaviour of a coated component. Thus a careful microscopic inspection is suitable for the evaluation of the abrasion wear properties [34, 35].

Oscillating sliding wear is connected with tribo-chemical reactions like fretting corrosion and crack growth due to fatigue caused by cyclical tribological stress. These failures are relevant in many industrial applications from bearings to turbine blades or heat exchangers for power generation [36] and in the same way in miniaturized mechanical, optical and electronic devices. Studies on nickel dispersion coatings give evidence that strengthening by micron- und submicron-scaled particles of Al_2O_3, SiC or diamond is more effective than strengthening by Si_3N_4 or TiO_2 [27, 37, 38]. The friction coefficient is conditioned by the content and size of incorporated particles. For example, values between 0.29 (0.3 and 0.7 μm particle diameter) und 0.34 (5 μm particle diameter) were noticed for SiC and increasing particle concentration raised the friction coefficient, although not above 0.5 [37]. The abrasive effect of released particles in the contact zone is unfavourable, in particular in the case of square-etched micron-scaled particles. Therefore, the best properties will be expected for well-dispersed and nano-scaled particles.

Apart from vibration stress, complex dynamical loads occur to various degrees by cavitation in fluid-handling equipment like propellers, turbine pumps and pipelines where nickel composites can be employed as interesting corrosion/erosion-resistant layers. Nevertheless, there is little information pertaining to the effectiveness to resist cavitational stress. Corresponding investigations of electroless Ni-P-SiC have recently been published [39]. The cavitation test according to ASTM G32 is a well-established test developed for evaluating cavitation resistance. Materials are subjected to a combination of impact and fatigue stresses under the influence of a sonotrode. The erosion resistance of composites under cavitational load is correlated to the microstructure as well as the elastic and plastic properties derived from the instrumented indentation test. SEM studies on crack propagation are valuable to relate wear appearances and to detect particle-adherence failures.

Experimental

Deposition and particle characterisation. Nickel and nickel dispersion layers were electroplated on cold-rolled low-carbon steel in a Watts electrolyte (250 g/l $NiSO_4$, 30 g/l $NiCl_2$, 30 g/l H_3BO_3, 0.3 g/l $NaC_{12}H_{25}SO_4$) under following conditions: Cathode current density - between 200 and 1000 A/m², typically 400 A/m^2; temperature - 50-55 °C; pH value - 3.2-4.2; particle concentration - 5 or 20 g/l. Different experimental setups came into operation for the deposition. One experiment was carried out without ultrasound, i.e. under silent condition, and the electrolyte was stirred at 500 – 700 rpm in order to prevent the sedimentation of the solids content. Sonication was used additionally to avoid the agglomeration of particles during the deposition. For the application, an ultrasonic bath with a frequency of 35 kHz (Sonorex super, Bandelin) was used, which provides only a continuous mode of the sonic field. For continuous and pulse modes of the ultrasound application, the ultrasonic bath was replaced by an immersed sonotrode (with a frequency of 30 kHz) provided with an ultrasonic processor (UIP 250, Dr. Hielscher GmbH). Apart from pulsing (pulse range 0-100 %), modifying of the amplitude between 20 and 100 % (0.2-1) is possible by power control.

Table 1 Producer specification and phase analysis of the incorporated particles.

Particles	Size [µm]	Product / Producer	XRD analysis
TiO_2	0.021	P25, Degussa	Anatase, Rutile (4:1)
TiO_2	0.280	Tronox R-U-2, Kerr Mc Gee	Rutile
TiO_2	5-20	Amperit 782.8, H.C.Starck	Rutile (about 80 vol %)
SiC	0.040	diceram, Ceramic Components GmbH & Co. KG	Moissanite 6H, also Si_3N_4
SiC	0.550	Grade A 20, H.C. Starck	Moissanite 6H, 3C
SiC	5	LS127255MLE, Goodfellow	Moissanite 4H, 5H, 6H

Primarily, particles for incorporation were selected in view of their hardness and size: TiO_2 with a Mohs hardness between 5.5 for rutile and 6.5 for anatase (comparable to nickel, the Mohs hardness of which is around 5), and SiC with a remarkably higher Mohs hardness of 9.6. The particle size was selected under the aspect of influencing the matrix structure. Therefore micron-scaled particles (i.e. around 5 µm), submicron-scaled particles (i.e. around 0.5 µm) and nano-scaled particles (i.e. around 30 nm) from different producers were provided for incorporation. Size, shape and crystallographic phases were verified by SEM and XRD respectively. Titania particles mainly consist of rutile except for the nano-scaled particles with preponderance of anatase. Silicon carbide particles consist of different hexagonal and cubic polytypes. Table 1 summarizes the producers' size specifications and the phase analysis results by X-ray diffraction. SEM images of the powders reveal the diverse particle shapes; micron-scaled particles are fractured (Fig. 1a) and smaller particles are rounded (Fig. 1b). Strikingly, the latter tend to agglomerate. Aside from these features, the different electrical behaviour is mentionable with respect to the electroplating process of the matrix. Titania is isolating in contrast to semi-conducting silicon carbide.

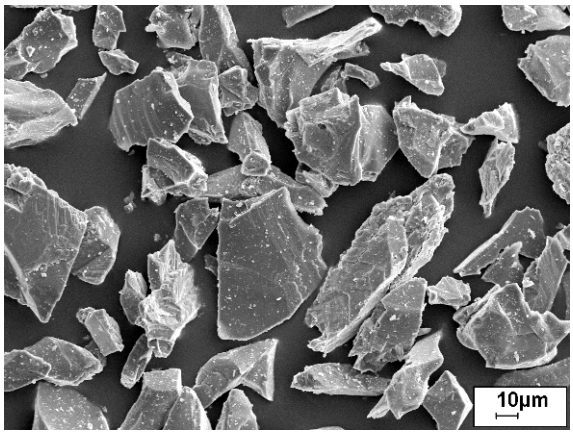

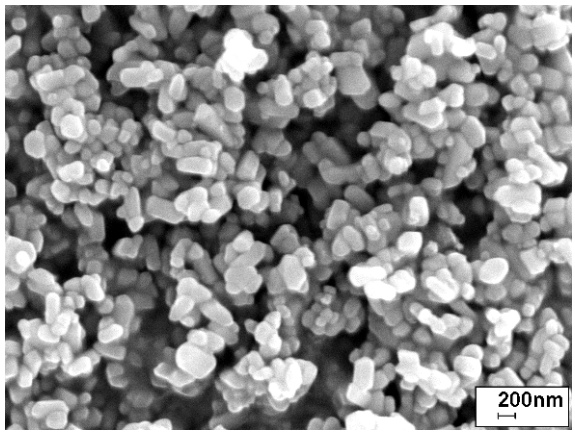

Fig. 1 Particles of different sizes and shapes.
Fig. 1a TiO_2 5-20 µm **Fig. 1b** TiO_2 280 nm

Microstructure characterisation. All X-ray diffraction experiments (XRD) were done in a D5000 (Siemens) diffractometer equipped with a Co Kα source and an Euler cradle for detailed texture studies. Residual stresses of first order were determined from the strains measured by X-ray diffraction. Scanning electron microscopic (SEM) images combined with energy dispersive X-ray spectroscopic studies were done in a LEO 1455VP equipped with an EDX detector (EDAX). Backscattered electron-beam diffraction (EBSD) data were collected in a Nova nano-SEM 2000 (FEI) equipped with a Nordlys II electron backscattering diffraction detector (Oxford Instruments) under the conditions of an acceleration voltage of 20 kV, a probe current of 6 nA, a 5000-fold magnification, a tilt angle of 70 ° and a grid spacing between 0.05 and 0.015 µm. Indexing (5 bands, 50 reflectors) and map creation as well as texture analysis was done by HKL CHANNEL 5 software. For grain size determination, the mean linear intercept method was used as an implement. Transmission electron microscopic (TEM) investigations were performed in a 200 kV CM20 (FEI) on Ar-ion-polished specimens in plan-view. SEM specimens were pressure-embedded in a conductible resin, mechanically grinded and OP-polished.

Electrochemical characterisation. For potentiodynamic measurements, small specimen were cut off the samples, contacted with a soldered wire and embedded in epoxy resin. A defined specimen surface (0.196 cm^2) was exposed to 0.1 mol NaCl solution at 25 °C. The polarisation curves were acquired in a conventional three-electrode corrosion cell (KMZ 3, Potentiostat PS6, Sensortechnik Meinsberg GmbH) according to DIN 50918. A saturated Calomel electrode was used as reference electrode and platinum as counter electrode. The tests were mainly conducted at a sweep rate of 0.5 mV/s, after 30 min, when the open circuit potential was stabilised. After the polarisation test, the corrosion appearance was observed and the volumetric corrosion was determined by digital fringe projection in a micro-optical 3D measuring device (MikroCAD compact, GFMesstechnik GmbH).

Hardness characterisation. An instrumented indentation tester (FISCHERSCOPE HM100) was employed for measuring the Martens hardness up to 500 mN (HM 0.5), the elastic indentation modulus and the share of plastic deformation of the composite layers.

Abrasion wear testing. Scratch testing equipment (REVETEST RST S/N 27-0445, CSM Instruments) was used for the evaluation of the abrasion wear behaviour. The critical load of the first failure appearance was detected by the observation of acoustic emissions during the progressive increase of the normal load on the scratching diamond stylus. The scratch energy density was determined for constant normal loads of 10, 50 and 100 N. Therefore, scratch widths and depths were measured subsequently by a profilometer (T 4000 Hommel). The failure topography was studied and compared by means of SEM images.

Oscillating sliding wear testing. Fretting was tested according to DIN 50324 by a ball-plane arrangement under controlled conditions (temperature - 22 °C, relative humidity - 50 %) with a tribometer SVT 40 (Dr.-Ing. Watzau Mess- und Prüfsysteme GmbH). Bearing balls (10 mm in diameter) were slided on the grinded layer surface with respect to a defined roughness of the plane. The normal load was 5 N, the oscillating frequency 20 Hz, the amplitude 1 mm. For 6,000 and 36,000 test cycles, the linear cumulative wear, the friction coefficient and the electrical resistance for indicating tribological oxidation were recorded. Similar to the measurement of the volumetric corrosion, the volumetric wear was determined by digital fringe projection in a microoptical 3D measuring device (MikroCAD compact, GF Messtechnik GmbH).

Cavitation wear testing. The cavitation erosion resistance was evaluated according to ASTM G32-92 (vibratory frequency - 20 kHz, peak-to-peak amplitude - 65 µm, temperature - 25 °C, normal pressure) using an ultrasonic device (UIP 250, Dr. Hielscher Ldt.). Apart from the oversized amplitude, an indirect test arrangement was used, which is a commonly used modification [40]. The test specimen was situated at a distance of 0.5 mm to the opposite vibrating sonotrode end face. The test was performed in distilled water on layer surfaces defined by fine grinding (grid 600). The total exposure time was 8 h; the incremental mass loss was measured every hour.

Results and discussion

Microstructure. After some refinement of understanding in structure-characteristic relations concerning the effect of substantial electroplating parameters, the Watts bath without additives was used deliberately for all nickel and nickel dispersion layers apart from sodium dodecyl sulfate. The large amount of nickel sulphate provided the necessary concentration of nickel ions. Nickel chloride improved the anode solubility and increased the conductivity of the electrolyte. Boric acid was used as a weak buffer to maintain pH. The wetting agent sodium dodecyl sulphate is an anionic surfactant which prevented the hydrogen vesicles from a longer adhering on the cathode surface and avoided hydrogen embrittlement. Electroplating parameters such as concentration, temperature and current density are known to affect the type of layer, i.e. transitions from the field-oriented isolation type (FI type) over the base-oriented reproduction type (BR type) and the field-oriented texture type (FT type) to the unoriented dispersion type (UD type), which was established in the Fifties by Fischer [41]. Nevertheless, for a pure Watts nickel solution, no significant change of the type of layer was registered for varying the current density [42] between 200 and 1000 A/m², which has confirmed that the Watts bath reliably generates reproducible coatings. Typically field-oriented films were observed by SEM imaging with backscattered electrons in the material contrast mode, which, moreover, reveals a remarkable orientation contrast for Ni crystals. At the interface to the substrate, the layer starts fine-crystalline with a thickness in the range of some microns. After forming the so-called initial layer, increasing columnar grains arise because of competitive growth (Fig. 2a-b).

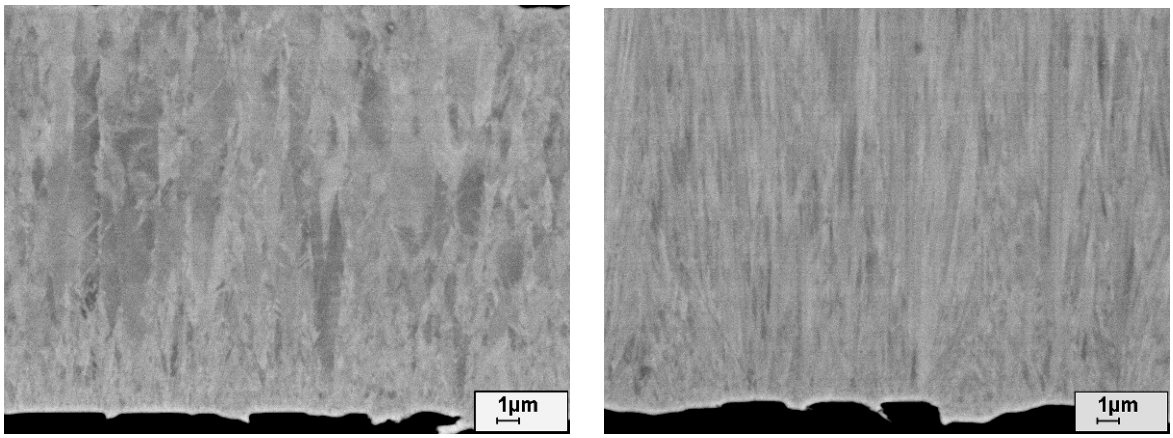

Fig. 2a-b Ni under silent (a) and sonicated (b) electroplating conditions.

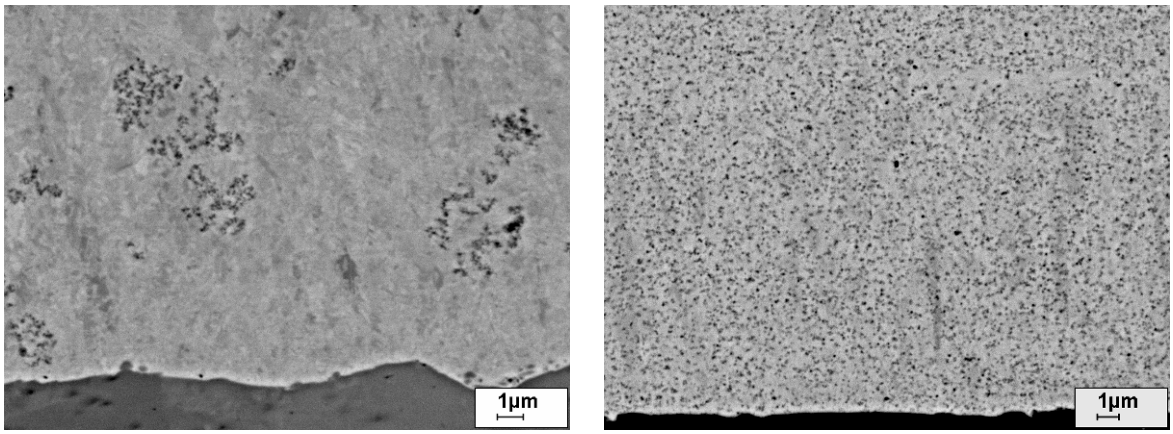

Fig. 2c-d TiO_2 Ni composite under silent (c) and sonicated (d) electroplating conditions.

The application of ultrasound has several effects on the appearance of nickel films. The columnar structure appears remarkably refined due to narrow grains with an increased aspect ratio. The preceding initial layer appears strikingly decreased, i.e. typically halved (Fig. 2b). Apart from sonication, the thickness of the initial layer or nucleation zone is influenced by the electroplating current density and seems to reach optimum conditions at 400 A/m^2 (Fig. 3). If submicron or nano-sized particles are incorporated, they are well-dispersed (Fig. 2d) and on the other hand immediately agglomerate under silent deposition conditions (Fig. 2c).

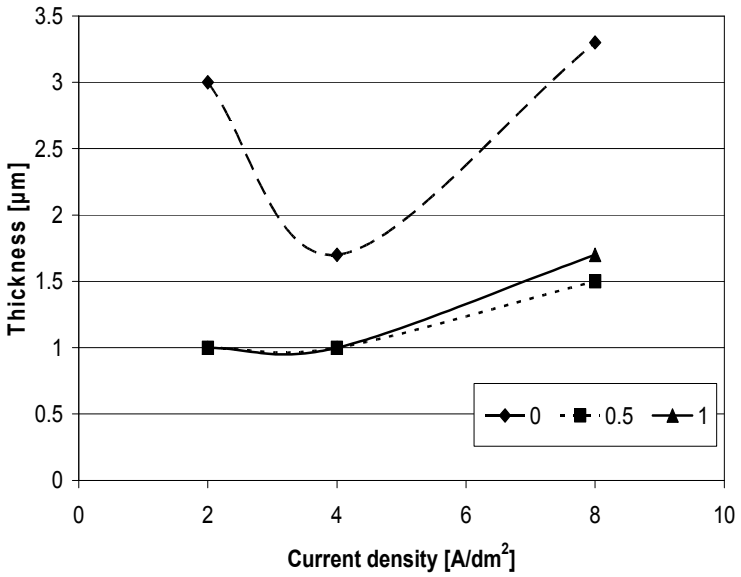

Fig. 3 Thickness of the initial layer of nickel electroplated under silent and ultrasound conditions (0 silent, pulse mode 0.5 equals half cycle, 1 equals full cycle of ultrasound).

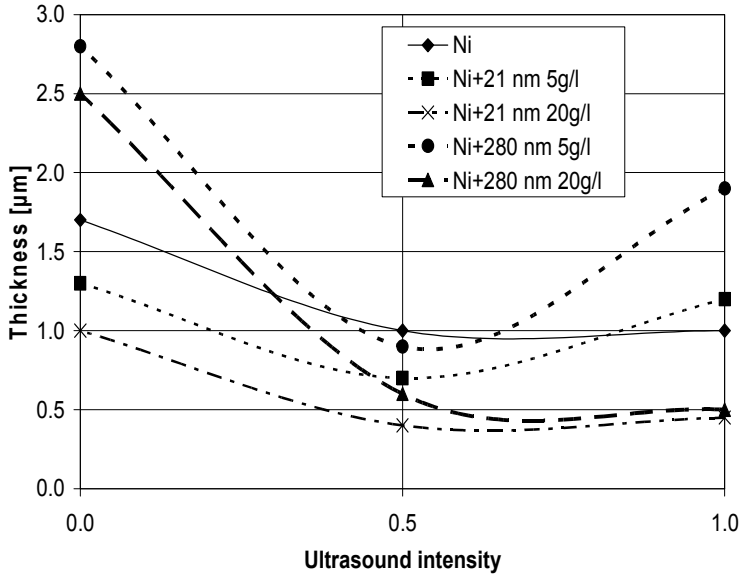

Fig. 4 Thickness of the initial layer of Ni-TiO_2 composites electroplated under different sonication modes (current density 4 A/m^2).

Even though no particles were incorporated into the initial layer between the substrate and the composite layer, the particle content in the electrolyte has decreased the thickness of the initial layer additionally to sonication. The higher the particle concentration and the lower the particle size the lower the initial layer thickness (Fig. 4). With well-dispersed nano-scaled particles under optimum conditions, which includes the proper choice of ultrasound intensity by adjusting the pulse cycle duration, a reduction of up to 200 nm was achieved. These results are of special interest with respect to the application in microsystems where the total thickness of the composite layers has to be downsized. In composites with incorporated agglomerates of nano-sized particles or with incorporated micron-scaled particles, the thickness of the initial layer remains unchanged compared to pure nickel layers.

Compared to electron backscattering images of nickel films, EBSD studies give a rather accurate picture of the grain size since EBSP quality maps are composed in terms of crystallographic orientation. Figure 5a shows the EBSP quality map of the interface region of a submicron TiO_2 nickel composite (left) on steel (right). After ignoring the Ni twins in the grain definition, a grain size map was composed (Fig. 5b) which clearly shows the already specified grain-size gradient from the initial layer (around 100 nm) to the Ni matrix with incorporated particles (300-700 nm). The white spots could not be indexed by face-centred cubic nickel. An EDX phase map processed by means of the phase cluster analysis reveals these spots as TiO_2 particles (Fig. 5c). By properly identifying all points and re-indexing inside each TiO_2 particle, a few pixels produce indexable patterns. In the corresponding map (Fig. 5d) small wire-frame drawings of the unit cells illustrate the orientation of the rutile particles in addition to the inverse pole figure (IPF) colour coding.

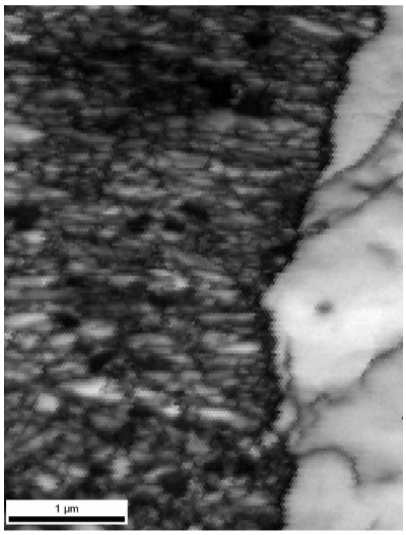

Fig. 5a EBSP quality map.

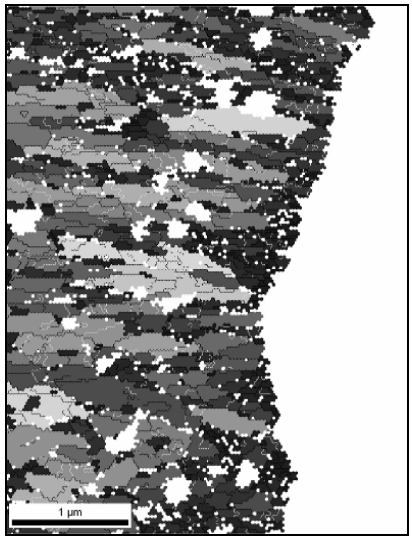

Fig. 5b Grain size map.

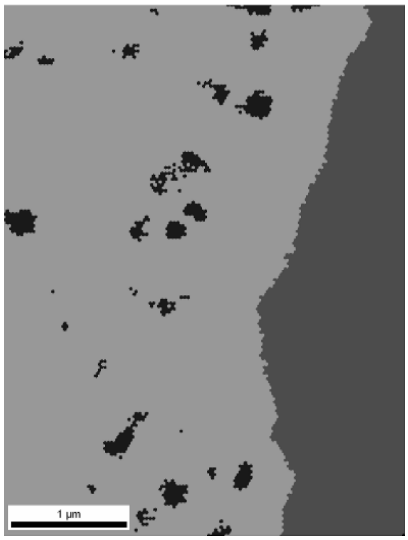

Fig. 5c EDX phase map:
TiO_2 particles (black),
nickel (light grey),
steel (dark grey).

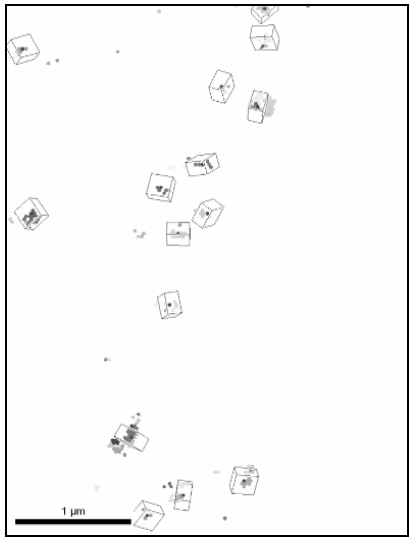

Fig. 5d IPF map of TiO_2 particles
with wire frame drawings of the unit cells.

Table 2 Nickel grain size of different composites.

Mean linear intercepts (MLI) transverse and in growth direction (GD) and derived aspect ratios.

Layer	MLI transverse GD [µm]	MLI in GD [µm]	Aspect ratio
Initial layer	0.27 ± 0.19	0.27 ± 0.19	1.0
Standard Watts Ni	0.49 ± 0.47	0.68 ± 0.73	1.4
Ultrasonic impact	0.38 ± 0.25	0.56 ± 0.60	1.5
Ni + 21 nm TiO_2	0.27 ± 0.23	0.28 ± 0.20	1.0
Ni + 280 nm TiO_2	0.36 ± 0.30	0.57 ± 0.87	1.6
Ni + 5-20 µm TiO_2	0.26 ± 0.19	0.33 ± 0.35	1.3
Ni + 550 nm SiC	0.28 ± 0.20	0.34 ± 0.38	1.2
Ni + 5 µm SiC	0.51 ± 0.26	0.66 ± 0.92	1.3

Table 2 summarizes the grain size parameters, i.e. mean intercepts and aspects, of the matrix in all examined nickel composite films. The data were collected near the substrate and the mean linear intercepts were determined in film-growth direction as well as normal to film-growth direction.

Table 3 Textures derived from XRD and EBSD examinations.

Layer	Texture (XRD)	Texture (EBSD)
Initial layer	No texture	No texture
Pure nickel (silent)	Fibre <211>	Fibre <211>
Pure nickel (US)	Fibre <110>	Fibre <110> + Fibre <100>
Ni + TiO_2 Ø 21 nm	Fibre <100> + Fibre <111>	Fibre <100> + Fibre <111>
Ni + TiO_2 Ø 280 nm, low concentration	Fibre <211>	Fibre <211> + Fibre <111>
Ni + TiO_2 Ø 280 nm, high concentration	Not measured	Fibre <100> + Fibre <111>
Ni + TiO_2 Ø 5-20 µm	No texture	No texture
Ni + SiC Ø 550 nm	Fibre <110>	Fibre <110>
Ni + SiC Ø 5 µm	Fibre <100>	Fibre <100>

The crystallographic orientation is summarized in Table 3, which compares matrix textures derived from XRD as well as EBSD results.

As stated above, pure nickel layers consist of columnar grains with an enhanced aspect ratio due to sonication. The incorporation of micron-scaled particles has different consequences with respect to the particles material. During their incorporation they act as new nucleation sites. Especially around strongly isolating TiO_2 particles, a large quantity of small equiaxed crystals grow similar to the initial layer and exhibit a decrease of the mean grain size. The columnar matrix growth is disturbed and no texture formation is established which is accompanied by a halved internal stress. The incorporation of semi-conducting SiC particles is initially connected with undisturbed grain growth until the particle is adsorbed on the newly developed surface. Solely on top of the particle, new crystals similar to the initial layer are formed as a new basis of continued columnar growth. Therefore, the mean grain size remains unchanged and a texture can develop in the matrix similar to pure nickel layers which typically reveal <100> or <211> fibre textures for medium current densities [42]. Again, residual stress is halved compared to pure nickel. The effect of remarkably different current distributions at the cathode due to conducting or non-conducting particles in the electrolyte is pointed out in a survey of different models of electrolytic co-deposition [5]. The texture formation of electroplated pure nickel can be summarized as follows: <100> oriented deposits originate from the free mode of growth; <110>, <210>, <111> and <211> fibre textures are induced by an inhibited process due to the presence of adsorbed hydrogen as well as hydroxyl groups [41, 43]. The application of ultrasound induces <110> fibre texture formation.

The incorporation of smaller particles below one micron results in a considerable grain refinement. SiC particles induce the <110> fibre texture similar to the texture in sonicated pure nickel layers. With increasing content, TiO_2 particles induce the development of the additional <111> fibre texture. Similar texture transformations as well as the development of additional texture components induced by particle incorporation are reported for Al_2O_3 [7], ZrO_2 [44], Y_2O_3 [45], SiC [46, 47]. Similar to sonicated pure nickel, changes of internal stress by incorporation of submicron- or nano-scaled particles (around 15 %) mostly remain in the limits of the mean value deviations (Table 4).

Table 4 Particle content in nickel composites.

Layer	Particle content in vol.-%	Residual stress [MPa]
Ni	0	370
Ni + US	0	370
Ni + TiO_2 Ø 21 nm, 5 g/l	1	420
Ni + TiO_2 Ø 21 nm, 20 g/l	3	380
Ni + TiO_2 Ø 280 nm, 5 g/l	4	310
Ni + TiO_2 Ø 280 nm, 20 g/l	4	420
Ni + TiO_2 Ø 5-20 µm, 20 g/l	13	160
Ni + SiC Ø 550 nm, 5 g/l	1	280
Ni + SiC Ø 550 nm, 20 g/l	7	410

In addition to residual stress, Table 4 reveals the particle concentration in the deposits outlined in terms of % by volume. The data are calculated from the measured Ti/Ni ratio and Si/Ni ratio assuming the stoichiometric composition, since light elements, especially carbon, can hardly be

analysed quantitatively by EDXS. The solids content increases with the size of incorporated particles and with an increasing amount of particles in the electrolyte and is affected by the rotation speed of the magnetic stirrer and the application of ultrasound as well as the pH-value of the electrolyte. The incorporation of micron-sized particles occurs homogeneously and without agglomerates under silent conditions; sonication even reduces the incorporation rate. Apart from micron-scaled particles, smaller particles immediately agglomerate during electroplating under silent conditions and unwanted agglomerates of substantial size are formed (Fig. 2c). The treatment with ultrasound during the coating process desagglomerates nano-sized particles as well as submicron-sized particles which, moreover, are partially reduced to smaller pieces.

The influence of ultrasound and incorporation of nanoparticles on the nickel matrix growth is shown as an examle in Figs. 6a-c. The growth direction of the composite film with TiO_2 particles of 21 nm diameter proceeds from right to left; only the first part (approximately one third) occurred under sonication which was switched off after some time (Fig. 6a).

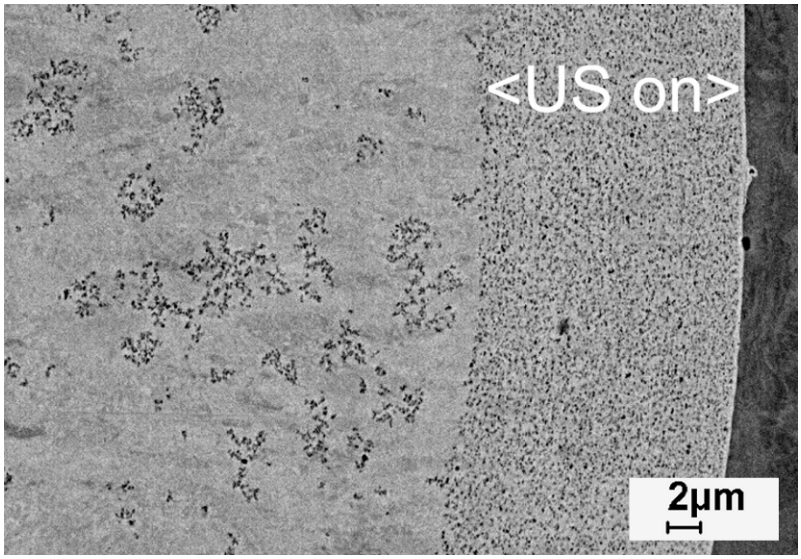

Fig. 6a Composite with 280 nm TiO_2 particles, partly sonicated.

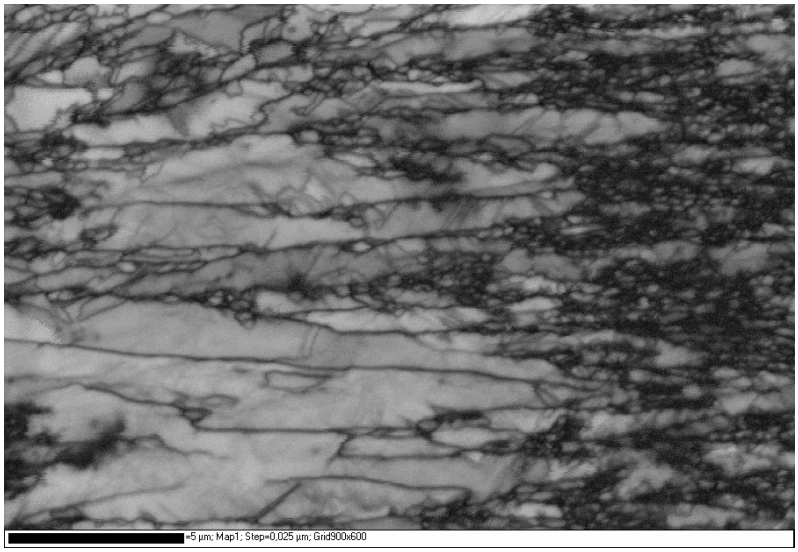

Fig. 6b EBSP quality map, marker 5 µm.

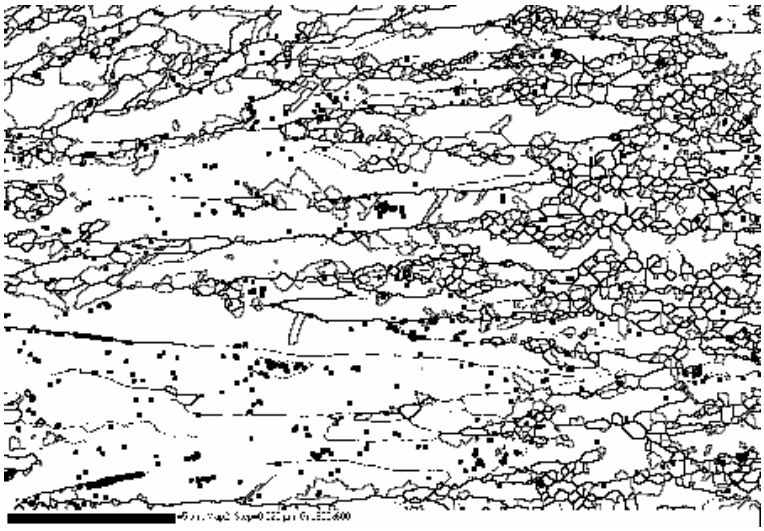

Fig. 6c Grain and phase boundaries, marker 5 μm.

Highly disordered crystals formed due to sonication are striking on the right side of the EBSP quality map with dark, i.e. low-band contrast (Fig. 6b). On the left side the EBSP quality map shows well-ordered columnar crystals in bright, i.e. high-band contrast developed under silent condition. In the corresponding grain boundary map (Fig. 6c), the transition from an increasing number of equiaxed tiny grains to large columnar grains is demonstrated by high-angle (black bold lines), low-angle (black thin lines) and twin (grey lines) boundaries of nickel grains. The particle distribution is reflected by black squares which appear scarce and dispersed on the right side but more frequent and concentrated on the left side. Low-angel boundaries seem to be induced by particle accumulation. As already mentioned, the particles can hardly be discovered and in this case only by incidental hits of the beam with single indexing per detected particle. Hence, the data collection does not reflect the real particle dimensions as well as the complete particle content and the portion of undetected particles is not known.

TEM studies were performed for the confirmation that TiO_2 nanoparticles are incorporated either monodisperse or in parts of small agglomerates under the influence of sonication. These particles (indicated by >) can be distinguished between tiny nickel crystals in the bright field image (Fig. 7). The inserted diffraction pattern shows nearly closed circles of the polycrystalline nickel matrix. The inner circle is attributed to the randomly arranged TiO_2 particles, more precisely to rutile. The beam incidence corresponds to the film growth direction; consequently the texture formation derived from EBSD pole plots cannot be observed.

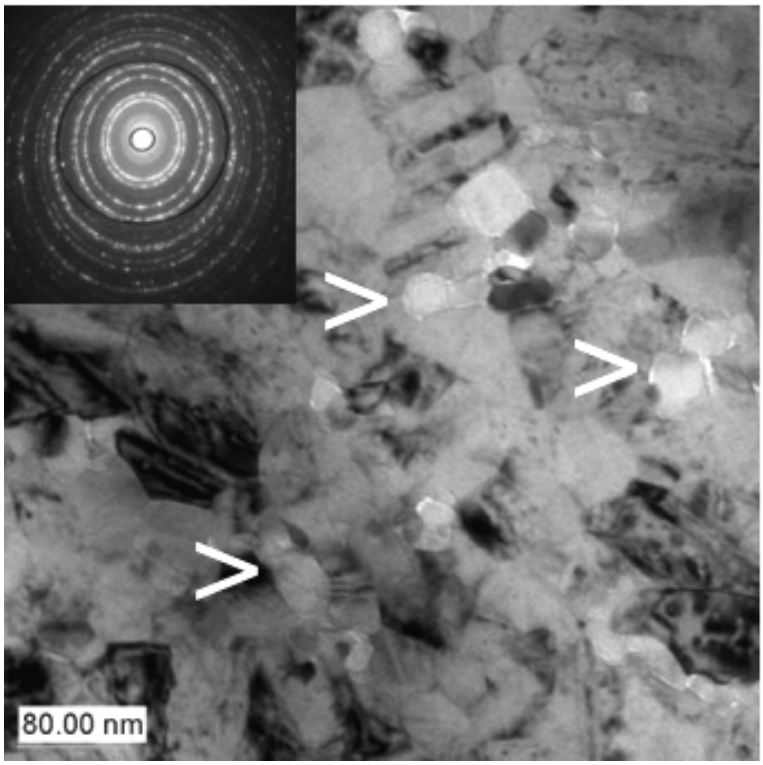

Fig. 7 TEM bright field and diffraction (insert) of TiO_2 particles (indicated by >) in nickel.

Corrosion behaviour. In comparison to the referenced nickel coating, the open circuit potential of examined dispersion coatings increases from -0.23 V up to -0.3 V (Fig. 8). This shift to a more cathodic range logically originates in the absorption of minor amounts of impurities from particle powders or incorporation of hydroxyl groups during electroplating. In contrast, the corrosion current density is slightly decreased by the incorporation of nano- and submicron-scaled particles (Fig. 9). Especially nano- and submicron-scaled TiO_2 show half of the corrosion current density, whereas the effect of micron- and submicron-scaled SiC remains in the range of the standard deviation. Micron-scaled TiO_2 particles provoke a clear rise of the corrosion current density with evidently wide deviation values.

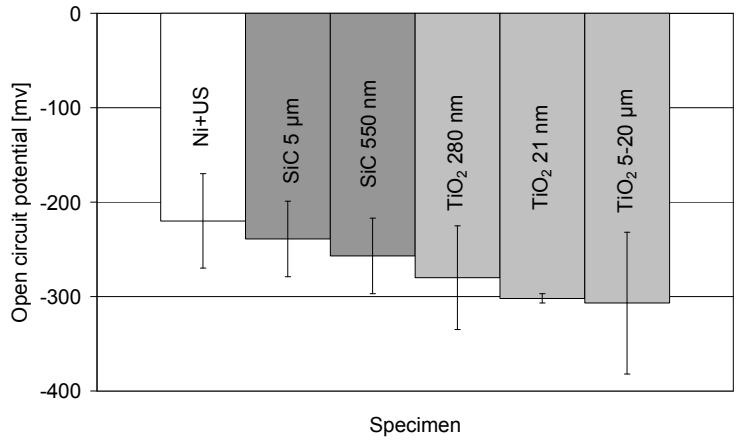

Fig. 8 Open circuit potential.

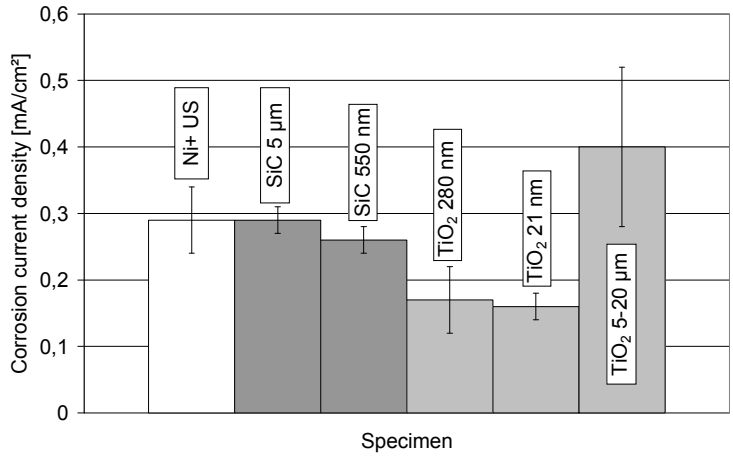

Fig. 9 Corrosion current density.

Compared to pure nickel, the minor decrease of the corrosion current density of composites with submicron- and nano-scaled particles corresponds with the increasing percentage of surface area occupied by the ceramic particles and confirms earlier results [17, 19]. Except for micron-scaled TiO_2-Ni composites, the corrosion current density of the nickel matrix itself seems not noticeably interfered with particle incorporation. Currently, substantial investigations are made on these nickel and nickel composites to gain deeper understanding of the measured corrosion data, especially of the differing standard deviation.

The total corrosion resistance of the composite can be evaluated more precisely in terms of corrosion appearances and mechanisms. Such evaluation was performed by 3D profiling for measuring the total corrosion erosion as well as the depth distribution of pits (Fig. 10-12). The measurements reveal pitting as the dominant corrosion appearance except for micron-scaled composites.

Submicron-scaled SiC (Fig. 10) gives rise to enhanced pitting corrosion with up to 75 % deep holes which cross the whole composite compared to nickel with 10 % pits crossing the layer. Related to the measured area of 9 mm^2, the total corrosion erosion by pitting is increased from 8 μm^3 for nickel to 10 μm^3. Similarly, the nano-scaled TiO_2 composite exhibits up to 42 % deep pits and a total erosion volume of 12 μm^3. The improved corrosion resistance shows the submicron-scaled TiO_2 composite (Fig. 11) with mainly shallow pits around 20 µm and a tenth part of decreased erosion volume of 1 μm^3.

Unlike semi-conducting SiC, the screening effect of TiO_2, i.e. the shielding of the matrix by dielectric particles seems to contribute to the favoured formation of shallow pits and minimizes the corrosion erosion volume. The incorporation of nano-scaled TiO_2 particles gives a lower effect of the lower solids content in the composite. The area of contact between the metal matrix and the corroding medium is not reduced sufficiently and the corrosion current is distributed inhomogeneously over the surface due to local corrosion elements. Aside from this aspect, the grain refinement due to nanoparticle incorporation produces an increased amount of grain boundaries acting negativly on the improvement of the corrosion resistance.

The incorporation of micron-sized particles changes the corrosion behaviour of the nickel composites substantially. Both the TiO_2-strengthened and the SiC-incorporated Ni layers show no corrosion holes (Fig. 12). The corrosion mechanism has completely changed to surface corrosion. Nevertheless, shallow pits may be masked due to the general corrosion. More detailed discussion is given in [48].

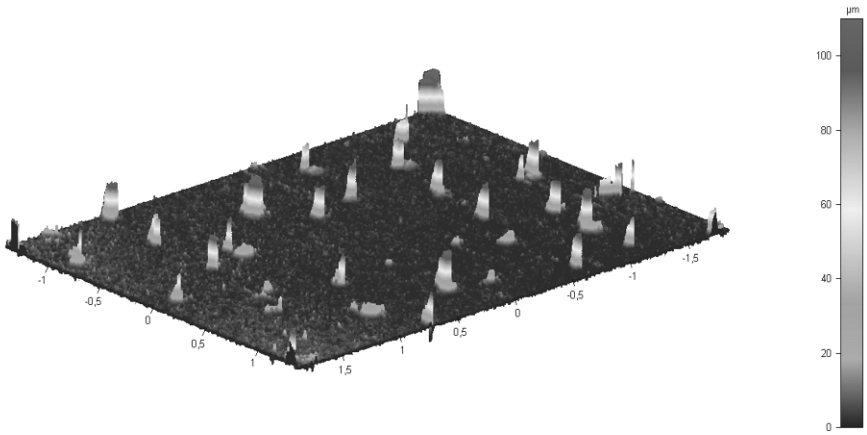

Fig. 10 Inverse 3D profile of a corroded 550 nm SiC-Ni composite.

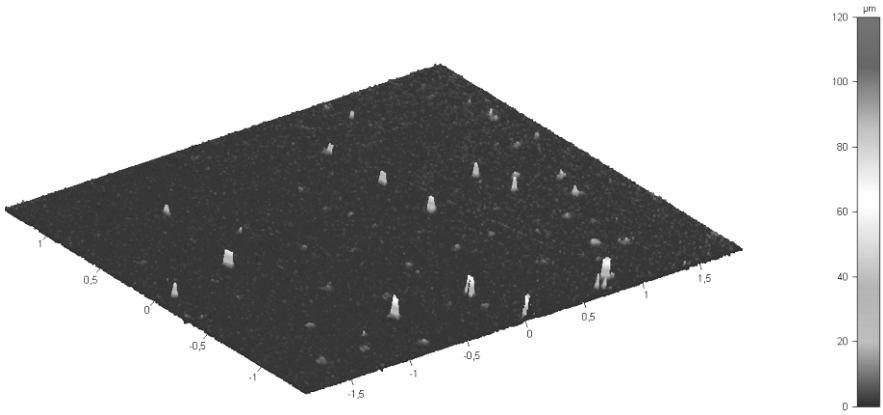

Fig. 11 Inverse 3D profile of a corroded 280 nm TiO_2-Ni composite.

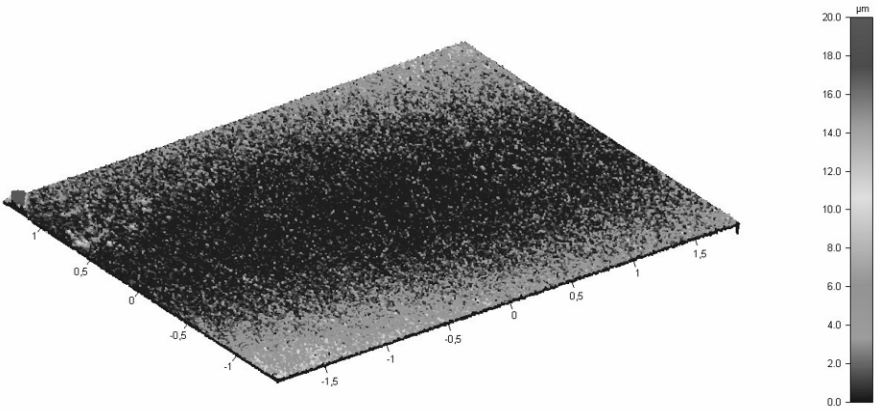

Fig. 12 Inverse 3D profile of a corroded 5 µm SiC-Ni composite.

Microhardness. Compared to composite layers, pure nickel layers generally show the lowest Martens hardness, whether standard or ultrasonically aided electroplating, which basically increases with increasing solids content. Figure 13 shows this general tendency marked by pointed lines, although a direct correlation was not found. A comparison with regard to the microstructure shows that the hardness is highest when the nickel grains are decreased by the incorporation of submicron

and, notably, nano-scaled particles (Fig. 14). Except for the different behaviour of the micron-scaled composites, grain refinement below 300 nm and particle distances below one micron suggest the considerable rise in hardness by dispersion hardening.

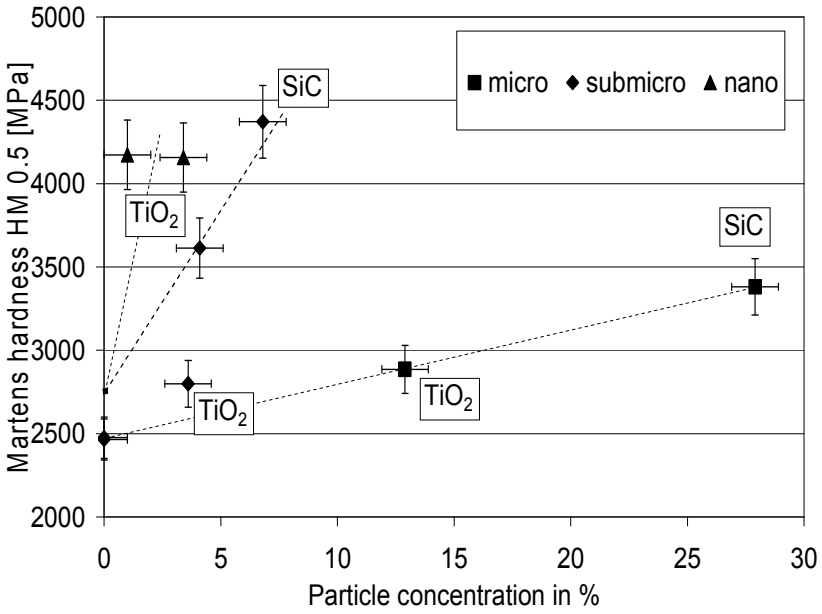

Fig. 13 Correlation of Martens hardness and particle content.

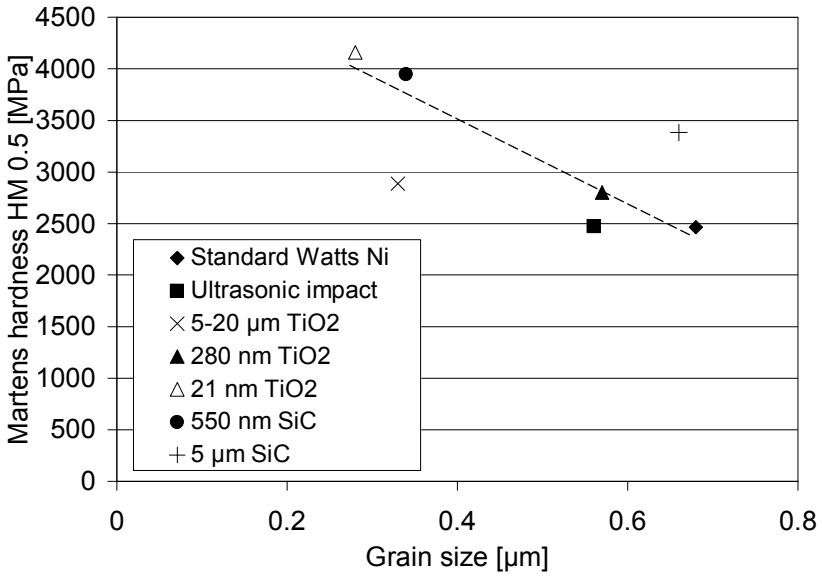

Fig. 14 Correlation of Martens hardness and nickel matrix grain size.

The instrumented indentation test provides the advantage of measuring supplementary mechanical properties such as the share of elastic deformation under indentation. Therefore, the fraction of plastic deformation as the quantity of formability of a material can be derived. Except for micron-scaled particles, the fraction of plastic deformation mostly decreases with increasing particle concentration and with decreasing nickel grain size. In the case of Ni-SiC micro-composites the plastic deformation fraction is similar to pure nickel and hence may be attributed to the similar microstructure of the matrix. The Ni-TiO_2 microcomposites have evidence of poor particle adherence and unoriented crystal growth which will be discussed as an exception later on. Figure 15

illustrates the relationship between particle content, particle size and the fraction of plastic deformation.

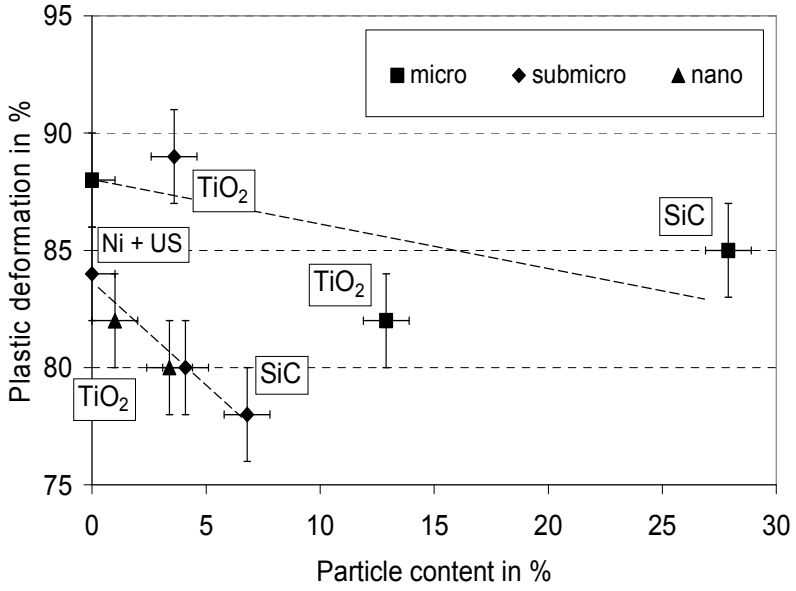

Fig. 15 Correlation of plastic deformability and particle content.

Abrasion wear. The scratch test primary developed for testing the adhesion of thin films is, moreover, suitable for the evaluation of the abrasion wear behaviour. With respect to composite layers, cracks and cohesive damage within the coating are convenient to evaluate the abrasion wear behaviour. A critical load can be determined by applying progressive load on the scratching diamond stylus and detecting acoustic emissions due to failure appearance. Additionally, the normal load, the friction force, the elastic and the plastic indentations are quantified.

A good criterion for the abrasion wear evaluation is the scratch energy density W_R [J/mm³], i.e. the ratio of the tangential force F_R [N] and the area A_R [mm²] of the cross section of the scratch obtained by measuring the scratch profiles after testing. Nickel shows the highest abrasion wear resistance for a normal load between 10 and 100 N when electroplated under ultrasound conditions (Fig. 16). The microstructure of such layers is determined by fine columnar grains with a high aspect ratio. According to the classic Hall-Petch law, grain boundaries act as obstacles to dislocation glide, and the yield stress for dislocation movement must be highest for smallest grain sizes. This is the case for the sonicated nickel and the nano-scaled composites where the application of a similar scratch necessitates a higher load. The yield stress below the indenter causes dislocation motions and no wear appearances can be detected at the bottom of the scratch.

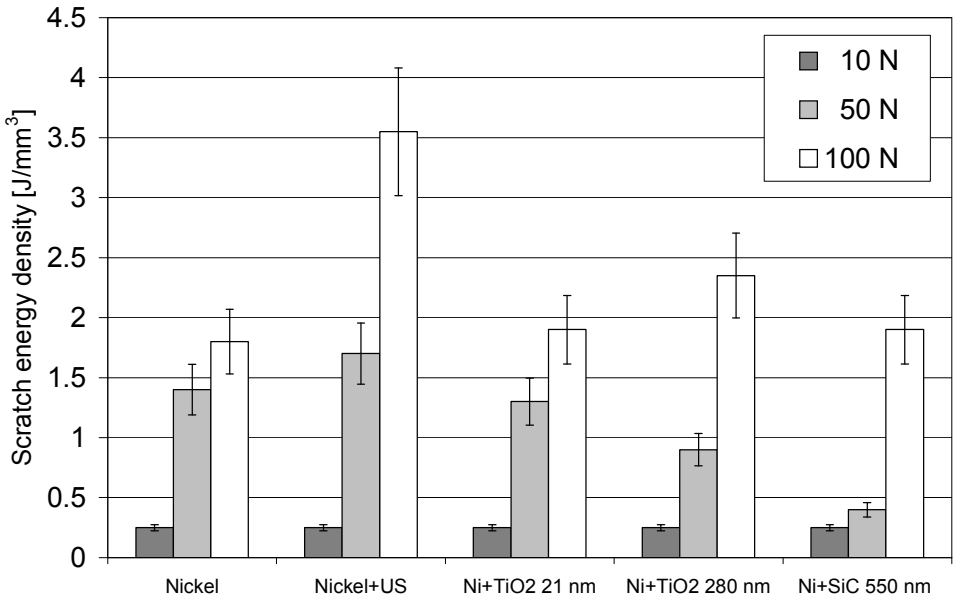

Fig. 16 Scratch energy densities of Ni and Ni composites for normal loads of 10, 50 and 100 N.

During the scratch test, different failure modes such as plastic deformation and chipping were distinguished by microscopic imaging. The scratch trace for a normal load of 10 N simply shows plastic deformation (Fig. 17a). Above 40 N, the plastic deformability is exhausted and, additionally, chipping with the formation of larger chips with increasing load is observed (Fig. 17b). Micron-scaled particles cause severe failures due to crack formation and particle debonding. Submicron SiC-strengthened nickel exhibits large chips due to the lowest plastic deformability of the composite whereas submicron- and nano-scaled TiO_2 composites show diminished chips lateral to the scratch traces. Plastic deformation zones can be observed on cross sections which are marked by the alignment of submicron- or nano-scaled particles (Fig. 18).

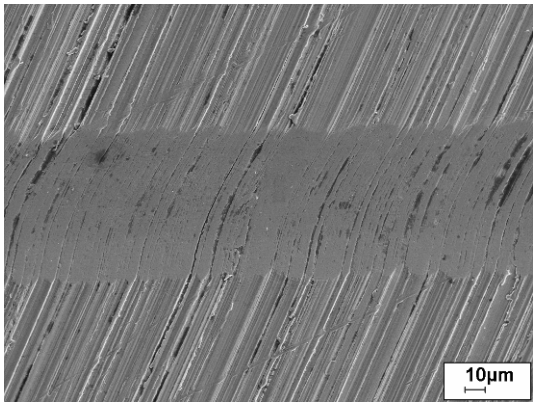

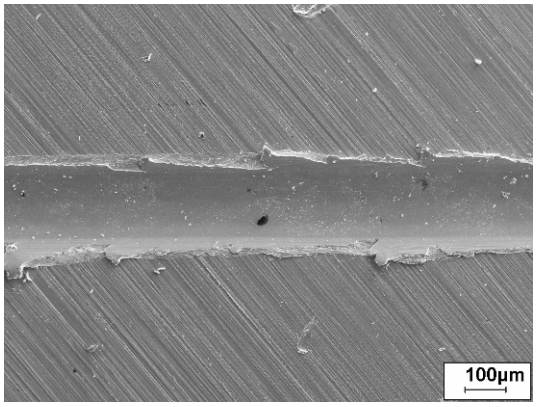

Fig. 17 Scratch traces on nickel layers.
a) Normal load of 10 N, SEM. b) Normal load of 100 N, LM.

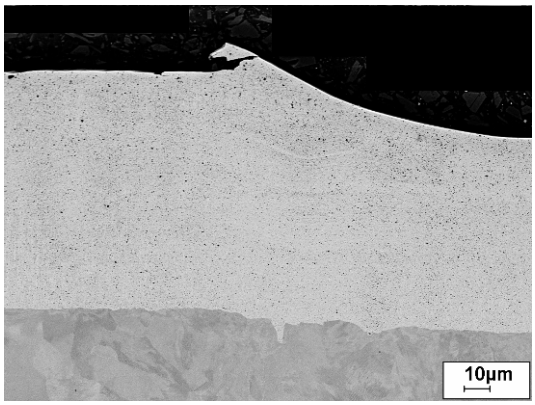

Fig. 18 Cross section of a scratch, 280 nm TiO_2-Ni composite, normal load of 50 N.

Fretting abrasion. Repeated cyclical rubbing between a steel ball and the composite surface mainly removes material from the composite, producing a wear calotte which was measured optically (Fig. 19, 20) giving the volumetric wear. Actually incorporated particles can be removed during the oscillating sliding and accelerate the abrasion process. The harder the particles are and the larger they are in size, the more they enhance abrading the composite surface (Fig. 21). Incorporation of nano- and submicron-scaled TiO_2 particles causes the lowest increase of wear which primarily can be attributed to the rounded shape of these particles. Crack growth by fatigue cannot be observed.

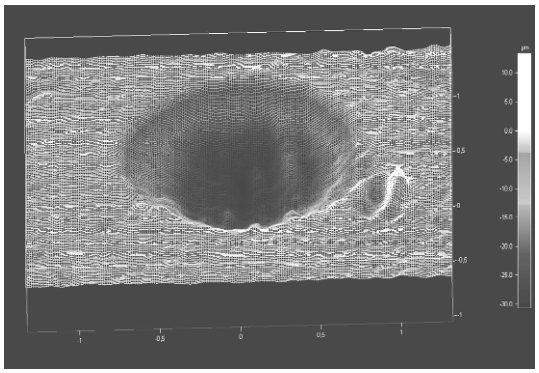

Fig. 19 Measuring the wear calotte.

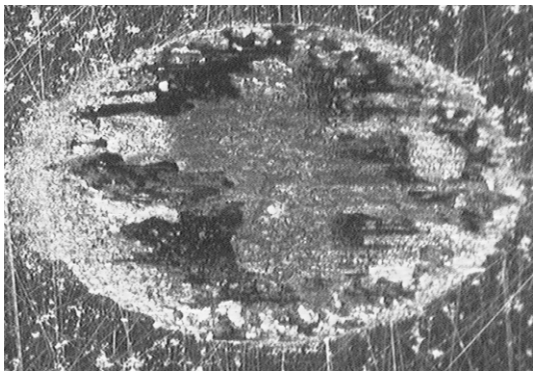

Fig. 20 Wear calotte on pure nickel.

The electrical resistance rises because of the formation of the tribo-oxidation layer after a short running-in period when the friction coefficient decreases. Small particles of this oxide layer as well as the actually incorporated particles are removed and rapidly abrade the oxide layer. Slight abrading as in the case of nano- and submicron-scaled TiO2 particles can exert a desirable cleaning effect if applicated as electric contacting materials. Detailed studies in comparison with electroless Ni-P layers are given in [50].

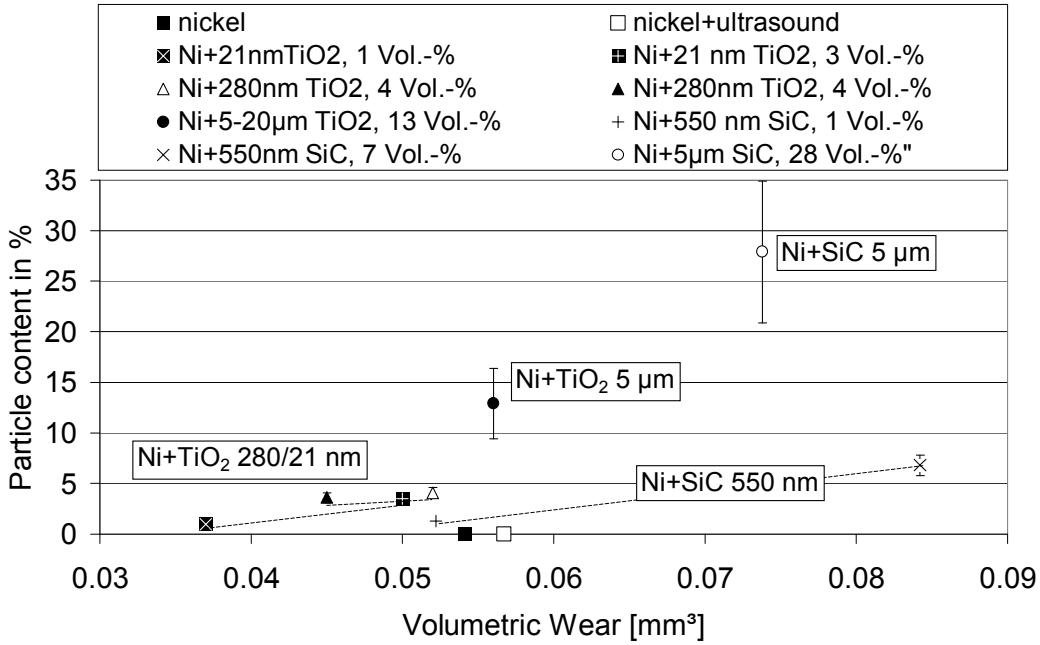

Fig. 21 Particle content and volumetric wear.

Cavitation wear. Contrary to other wear types, cavitation wear cannot be realised at the beginning. Invisible changes like lattice defects and distortions occur during the incubation period. The variety of cyclic events accumulates stress and initiates dislocations, causes work hardening, fatigue and cavitation pits. The surface region will be deformed, ductile fracture failure or brittle fracture failure occurs depending on materials behaviour. In [51] the pit formation is suggested in the following way: The collapse of the cavitation cloud causes a shock wave that spreads in the fluid and is damped. As the shock wave reaches the solid surface, single bubbles on it begin to oscillate and a micro-jet phenomenon occurs. The high-velocity liquid jet hits the solid surface and causes damage by single pits. Under cyclic loading the initiated cracks propagate and form a network.

The appearance of the partially eroded surface is shown in Figure 22. When the cracks propagate, they provoke discrete regions near the surface to be ejected as debris. The nickel matrix shows a ‘honeycomb’ appearance by mainly ductile fracture failures which are decreased by the incorporation of particles. For example, a micron-scaled SiC-strengthened composite is shown after eight hours of cavitation testing. In comparison to the initial state of the untreated sample (Fig. 23) the cross section (Fig. 24) and the surface (Fig. 25) of the treated sample illustrate the erosion after the test.

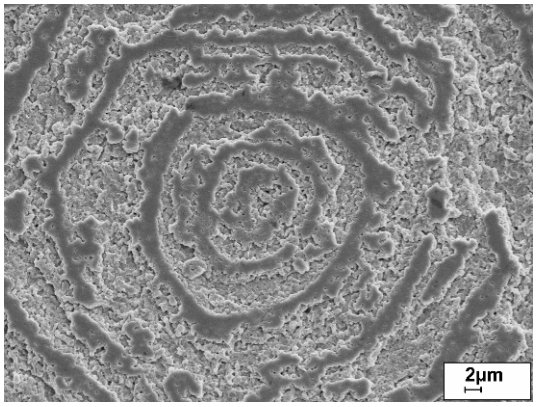

Fig. 22 Partially eroded surface.

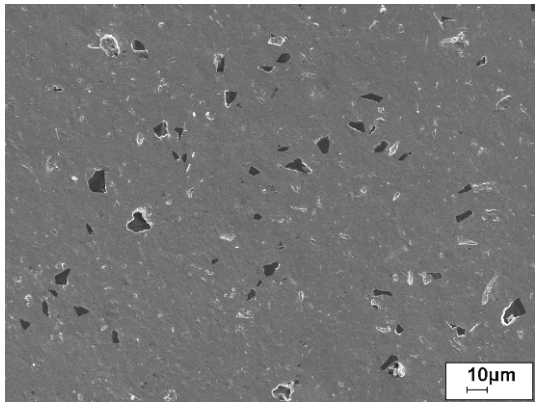

Fig. 23 Untreated surface.

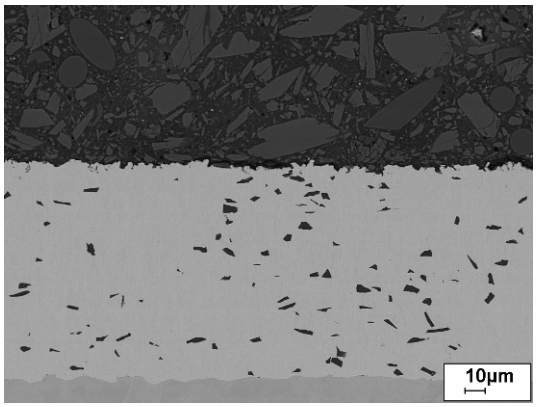

Fig. 24 Cross section of the eroded area.

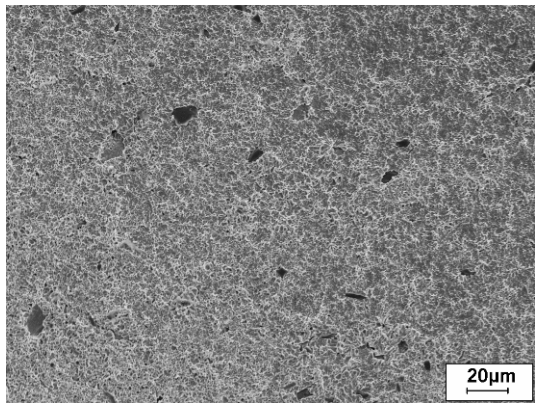

Fig. 25 Eroded surface.

Ni-SiC composite layers show a remarkably improved wear resistance in the case of micron-scaled as well as submicron-scaled particles. Only small pitting and shallow cracks can be observed after eight hours testing time. In contrast, nickel with micron-scaled TiO_2 shows severe erosion. Scanning electron microscopic imaging of the peripheral erosion zone shows the low adherence of the particles (Fig. 26). Perhaps this is reflected in the low residual stress of this composite (Table 4) and the unoriented crystal growth around the particles (Fig. 27). Due to these adherence failures, particles can easily be ejected by increasing cavitation stress which occurred in the centre of the affected region (Fig. 28). Erosion then proceeds in the holes, i.e. at the noticeably enhanced surface and quickly degrades the surrounding nickel matrix (Fig. 29).

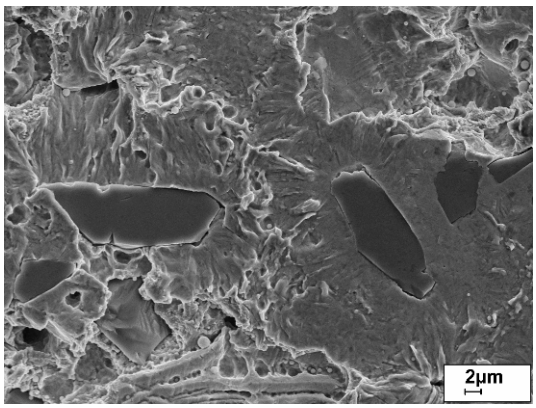

Fig. 26 Loosened TiO_2 particles.

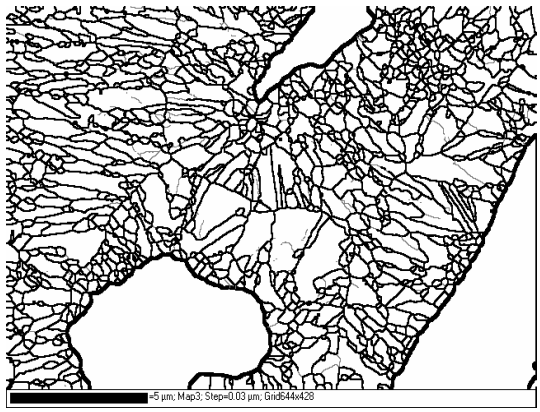

Fig. 27 EBSD-derived grain boundary map, marker 5 µm.

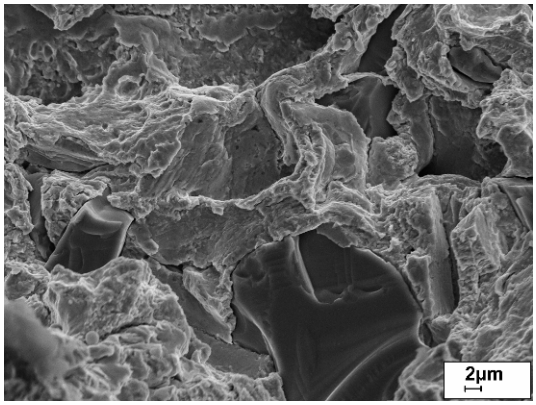

Fig. 28 Partly detached TiO_2 particles.

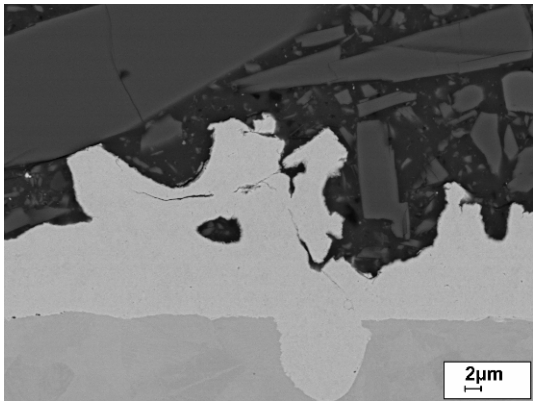

Fig. 29 Detached TiO_2 particles and severe erosion.

A direct comparison of the cavitation resistance between different materials permits the mean depth of erosion to be determined during an exposure or testing time of some hours (typically eight). The mean depth of erosion is determined as the average thickness of material removed from a specified surface area and was calculated by dividing the measured mass loss by the density of bulk nickel and the damaged surface area. Figure 30 demonstrates the progress of erosion by cavitation wear during a test period of eight hours.

Remarkably low erosion is measured for the submicron SiC-strengthened composite whereas the effect of micron-scaled SiC particles as well as submicron and nano-scaled titania particles is noticeable and similar. The pronounced wear resistance of submicron-scaled SiC nickel is similar to recently published results for electroless Ni-P coatings where the incorporation of SiC particles greatly reduced the occurrence of pitting. Nanoparticles provide the greatest cavitation erosion resistance, and appear to inhibit the onset of erosion damage [53]. Moreover, this is in accordance with the presented results, especially the remarkable performance of the nano-scaled TiO_2 composites.

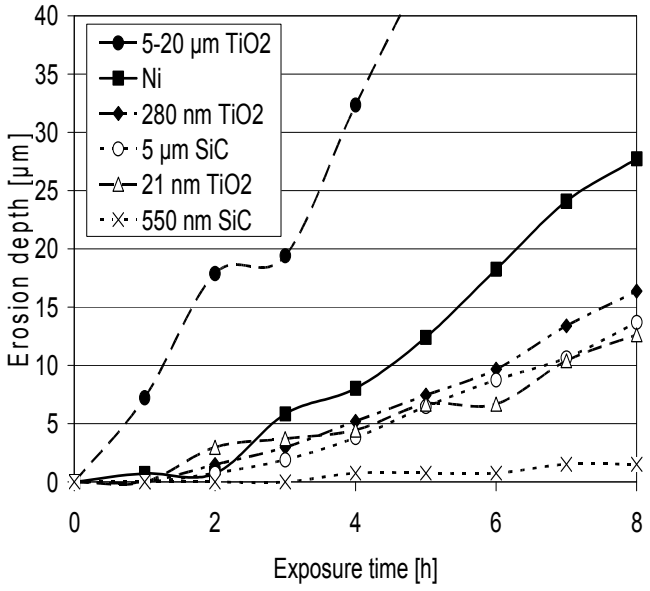

Fig. 30 Progress of erosion during the testing time.

Based on the mean depth of erosion, the corresponding erosion rate can be calculated. The maximum rate of erosion was regularly reached during the last two hours of the full testing time of eight hours. During the first hours the mean erosion rate clearly revealed some notable differences in incremental increase. Typically, three stages can be distinguished. During the initial or incubation stage, no material loss is observed. The incubation period, i.e. the intercept on the time axis of an extension of the maximum slope of the erosion-time curve, ranges from a few minutes for pure nickel and nickel with incorporated micron-scaled rutile to 3 hours for silicon carbide-strengthened layers. In the second phase, called acceleration stage, mass loss starts, which is expressed by a rapid rise of the erosion rate. Again, pure Watts nickel and even more nickel with incorporated micron-scaled TiO_2 show this behaviour extremely pronounced. Finally, the third phase, the maximum rate stage, is characterised by constant erosion with a constant erosion rate.

The cumulative mass loss as well as the maximum erosion rate are appropriate as representative numbers for the comparison of cavitation tests under the same conditions. Discussed in relation to the Martens hardness of the tested coatings (Fig. 31), a correlation between increasing hardness and decreasing mass loss by cavitation wear can be confirmed, which has been suggested formerly [52]. The composite with micron-scaled TiO_2 particles which suggests a failure mechanism distinctive to the other layers represents a striking exception.

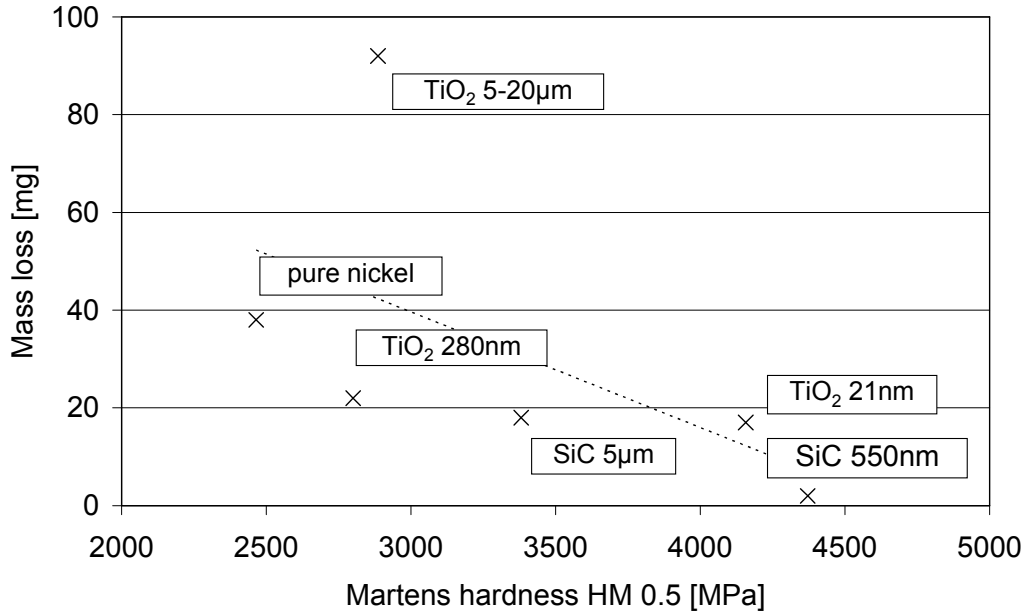

Fig. 31 Cumulative mass loss in correlation to Martens hardness.

The above-mentioned mechanism is based on the assumption of one-dimensional material removal, while cavitation wear is a three-dimensional process leaving a sponge-like structure or a so-called 'honeycomb' appearance. For that reason, mass loss and erosion rate results have to be discussed in terms of actual failure mechanisms of the composite layers, which has been done in detail elsewhere [54].

If particle-matrix bonding is adequate, the cavitation wear resistance is mainly correlated with the Martens hardness of the composite. Consequently, the good performance of nickel composites with nano-scaled TiO_2 particles is comprehensible due to the smallest mean grain size and a narrow grain size distribution of the matrix with the consequence of improved hardness.

Summary

Microstructure. The structural conditions of the nickel dispersion coatings vary despite constant electroplating conditions (current density, temperature, solids content of the suspension, agitating speed, pH-value) due to sonication and the material and size of the incorporated particles. The typical columnar structure of pure electroplated nickel films is refined by means of low-frequency ultrasound in the range from 20 to 400 kHz.

The incorporation of micron-sized titanium oxide particles generates additional nucleation surfaces for the film growth in contrast to semi-conductive silicon carbide particles. This is caused by the decreased current between cathode and shielding TiO_2 particles, whereas SiC particles leave the current distribution fairly unchanged. As a consequence, micron-scaled SiC is characterised by a good adhesion of the particles to the matrix contrary to micron-scaled TiO_2. Nanoparticle incorporation takes place inside the crystals as well as between grains and provokes improved grain refinement and quite different texture transitions with respect to pure ultrasonic nickel plating. The application of low-frequency ultrasound in the range from 20 to 400 kHz facilitates good particle dispersion in the electrolyte. The incorporation of different particles with respect to different materials and sizes proved to meet different demands with respect to corrosion and wear resistance.

Corrosion. The corrosion behaviour of the nickel dispersion coatings is dominated by the solids content. The electrolytic co-deposition of submicron-scaled TiO_2 and SiC particles with nickel leads to a reduced corrosion current density in 0.1 mol chloride solutions with an increasing percentage of surface area occupied by the ceramic particles and a reduction of the active nickel matrix area under corrosion testing. The screening effect of the dielectric TiO_2 particles contributes to the favoured formation of shallow pits and the erosion volume by corrosion is minimized. The incorporation of nano-scaled TiO_2 is counterproductive because of an increased amount of grain boundaries and enhances pitting. Nickel with micron-scaled particles exhibits a change in the corrosion mechanism from pitting to surface corrosion. Submicron TiO_2 is best for enhancing the corrosion resistance of composites.

Hardness. Apart from micron-scaled particles, an increased Martens hardness can be observed which is directly associated with a decreased grain size of the nickel matrix due to submicron and nanoparticle incorporation. The rise averages 20-60 %; correspondingly, the plastic deformability is slightly decreased by 10 %. Sonication and particle down-sizing result in matrix grain refinement and dispersion hardening.

Abrasion wear. For low normal loads (10 N) plastic deformation dominates and no differences can be measured between standard pure nickel and composite layers. With a rising normal load (40 N) chipping is additionally observed. Micron-scaled particles cause severe failures due to crack formation and particle debonding. For composites with smaller particles, a decrease of the scratch energy compared to Watts nickel is observed which can be correlated to the higher elastic deformability (i.e. lower plastic deformability) of the matrix. With further increasing the load up to 100 N, the scratch energy density remarkably rises in submicron- and nano-scaled composites due to strain hardening. Nevertheless, nickel electroplated under sonication provides the best performance.

Oscillation sliding wear. The dominant mechanism of oscillation sliding wear of pure nickel layers is tribo-oxidation. In nickel composites with incorporated particles, abrading by oxidised matrix particles as well as by detached particles appears. The latter is higher for square-etched particles and lower for rounded particles. It stands to reason that nano- and submicron-scaled TiO_2 particles cause the lowest volumetric wear. Slight abrading of the tribo-oxidation layer can be desirable in applications as electric contacting materials. Nano-scaled TiO_2 proved to be best for oscillation sliding wear resistance.

Cavitation wear. Due to cavitation stress, fatigue cracks develop and propagate along boundaries of columnar nickel grains in pure nickel films. Ductile fracture failures dominate. By the incorporation of particles, fatigue crack propagation is hindered and the erosion damage occurs evenly on the surface, provided that particle-matrix bonding is sufficient. The cavitation wear

resistance of nickel composites is improved especially by submicron SiC. Such composites show a tenfold wear resistance compared to nickel layers.

Acknowledgements.

We like to thank the following co-workers of the Institute of Composite Materials and Surface Technology for careful investigations and helpful discussions: Dr. H. Podlesak for TEM, G. Fritsche for XRD, E. Benedix for electrochemical corrosion studies and A. Leopold for wear testing. We gratefully acknowledge the cooperation with Prof. M. Hietschold, Solid Surfaces Analysis, Institute of Physics, and the technical assistance of his staff, and with Dr. Hielscher Ltd., Teltow, providing the sonotrode used for cavitation investigations. For comparative EBSD studies we thank Dr. René de Kloe from EDAX.

References

[1] A. Hovestad and L.J.J. Jansen: J. Appl. Electrochem. 25 (1995), p. 519.

[2] Y. Müller, P. Schmutz, Th. Lampke and A. Leopold: Metalloberfläche 60 (2006) 6, p. 40.

[3] C. Kerr, D. Barker and F. Wattslsh: Trans. Inst. Met. Finish. 78 (2000) 5, p. 171.

[4] N. Guglielmi: J. Electrochem. Soc. 119 (1972) 8, p. 1009.

[5] J.P. Celis, J.R. Roos, C. Buelens and J. Fransaer: Trans. Inst. Met. Finish. 69 (1991) 4, p. 133.

[6] E. Broszeit, G. Heinke and H. Wiegand: Metall 25 (1971), p. 470.

[7] B. Wielage, S. Steinhäuser, Th. Lampke, U. Hofmann and C. Jakob: Metalloberfläche 57 (2003), p. 25.

[8] W. Ruythooren, K. Attenborough, S. Beerten, P. Merken, J. Fransaer, E. Beyne, C. Van Hoof, J. De Boeck and J.P. Celis: J. Micromech. Microeng. 10 (2000), p. 101.

[9] K.S. Teh, Y.T. Cheng and L. Lin: J. Micromech. Microeng. 15 (2005), p. 2205.

[10] M.E. Hyde and R.G. Compton: J Electronal Chem 531 (2002), p. 19.

[11] S.H. Yeo, J.H. Choo and K.H.A. Sim: J. Micromech. Microeng. 12 (2002), p. 271.

[12] C.E. Brennen: *Cavitation and Bubble Dynamics*. Oxford University Press, New York 1995. ISBN 0195094093. Official Persistent URL.

[13] A. Tiehm, K. Nickel and U. Neis: Wattst. Sci. Tech. 36 (1997) 11, p. 121.

[14] Th. Lampke, B. Wielage, D. Dietrich and A. Leopold: Appl. Surf. Sci. 253 (2006) 5, p. 2399.

[15] S.L. Kuo, Y.C. Chen, M.D. Ger and W.H. Hwu: Mat. Chem. Phys. 86 (2004), p. 5.

[16] K. Kobayashi, A. Chiba and N. Minami: Ultrasonics. 38 (2000), p 676.

[17] B. Szczygiel and M. Kolodziej: Trans. Inst. Met. Finish. 83 (2005) 4, p. 181.

[18] S. Steinhäuser, B. Wielage and Th. Lampke: Physico-Chemical Mechanics of Materials, 4 (2004), p 489.

[19] I. Garcia, A. Conde, G. Langelaan, J. Fransaer and J.P. Celis: Corros. Sci. 45 (2003), p. 1173.

[20] S. Steinhäuser and B. Wielage: Surf. Eng. 13 (1997), p. 289.

[21] V. Medeliene: Surf. Coat. Technol. 154 (2002), p. 104.

[22] N.K. Shrestha, K. Sakurada, M. Masuko and T. Saji: Surf. Coat. Technol. 140 (2001), p. 175.

[23] I. Benea, P.L. Bonora, A. Borello and S. Martelli: Wear 249 (2002), p. 995.

[24] N. Periene, A. Cesuniene and L. Taicas: Plating Surf. Finish. 80 (1993), P 73.

[25] C. Malak: Metalloberfläche 48 (1994) 4, p. 232.

[26] E. Gnass: Metalloberfläche 54 (2005) 5, p. 26.

[27] I. Garcia, J. Fransaer and J.-P. Celis: Surf. Coat. Technol. 148 (2001), p. 171.

[28] L. Benea, R.L. Bonora, et al.: Mater. Corros. 53 (2002) 1, p. 23.

[29] F. Erler, C. Jacob, H. Romanus, et al.: Electrochim. Acta 48 (2003), p 3063.

[30] E.W. Brooman: Galvanotechnik 12 (2005), p. 2843.

[31] L. Du, B. Xu and S. Dong, et al.: Wear 257 (2004), p 1058.

[32] D. Kalyanaraman: Bull. Electrochem. 5 (1989) 9, p. 700.

[33] B. Reinhold: *Ein Beitrag zur Charakterisierung und zur Bewertung des Abrasionsverhaltens von Verschleißschutzschichten.* Dissertation, TU Karl-Marx-Stadt, 1990.

[34] K. Taube: Mat.-wiss. und Werkstofftechnik, 31 (2000), p 616.

[35] P.J. Burnett and D.S. Rickerby: Thin solid films, 154 (1987), p. 403.

[36] R. Junghans and J. Neukirchner: 13th International Colloquium Tribology, Ostfildern January 2002, Proceedings Vol. 3, p 1959.

[37] L. Du and B. Xu: Wear, 257 (2004) 9/10, p. 1058.

[38] S. Steinhäuser, Th. Lampke and B. Wielage: Materialwiss. und Werkstofftech. 34 (2003), p. 633.

[39] C.J. Lin, K.C. Chen and J.L. He: Wear 261 (2006) 11-12, p. 1390.

[40] D. Drozdz, R.K. Wunderlich and H.-J. Fecht: Wear 262 (2007) 1-2, p. 176.

[41] H. Fischer: *Elektrolytische Abscheidung und Elektronenkristallisation in Metallen*, Springer-Verlag, Berlin 1954.

[42] Th. Lampke, S. Steinhäuser, D. Richter and B. Wielage: Mat.-Wiss. u. Werkstofftech. 38 (2007) 1, p. 23.

[43] J. Amblard, I. Epelboin, M. Froment and G. Maurin: J. Appl. Electrochem. 9 (1979) 2, p. 233.

[44] B. Wielage, H. Podlesak, S. Steinhäuser and D. Nickelmann: Mess- und Prüftechnik 52 (1998), p. 386.

[45] M. J. Pomeroy and V. J. Cunnane: J. Electrochem. Soc. 150 (2003) 5, p. 356.

[46] C.S. Lin and K.C. Huang: J. Appl. Electrochem. 34 (2004), p. 1013.

[47] B. Szczygiel: Metalloberfläche 48 (1994), p. 239.

[48] Th. Lampke, A. Leopold, D. Dietrich, G. Alisch and B. Wielage: Surface and Coating Technology, 201 (2006), p. 3510.

[49] Th. Lampke, A. Leopold, D. Dietrich, H. Podlesak, G. Alisch, S. Steinhäuser and B. Wielage: Tagungsband WTK 2006, Chemnitz, 7.-8. 09. 2006, p. 483.

[50] Th. Lampke, A. Leopold, D. Dietrich, H. Podlesak and B. Wielage: Mat.-wiss. u. Werkstofftech. 37 (2006) 12, p. 1039.

[51] M. Dular, B. Stoffel and B. Širok: Wear, 261 (2006) 5-6, p. 642.

[52] J. K. Kristensen, I. Hansson and K. A. Morch: J. Phys. D: Appl. Phys. 11 (1978), p. 899.

[53] P. Prasad: J. Mat. Scie. Lett. 12 (1993), p. 902.

[54] Th. Lampke, D. Dietrich, A. Leopold, G. Alisch and B. Wielage: Surface and Coating Technology (2008) accepted.